Energy & Environmental Science



PAPER

View Article Online
View Journal | View Issue



Cite this: *Energy Environ. Sci.*, 2014, **7**, 779

# Photoelectrochemistry of core–shell tandem junction n–p$^+$-Si/n-$WO_3$ microwire array photoelectrodes†

Matthew R. Shaner,[ab] Katherine T. Fountaine,[ab] Shane Ardo,[a] Rob H. Coridan,[a] Harry A. Atwater[bc] and Nathan S. Lewis*[ab]

Received 10th September 2013
Accepted 7th November 2013

DOI: 10.1039/c3ee43048k

www.rsc.org/ees

Tandem junction (n–p$^+$-Si/ITO/$WO_3$/liquid) core–shell microwire devices for solar-driven water splitting have been designed, fabricated and investigated photoelectrochemically. The tandem devices exhibited open-circuit potentials of $E_{oc} = -1.21$ V *versus* $E^{0\prime}(O_2/H_2O)$, demonstrating additive voltages across the individual junctions (n–p$^+$-Si $E_{oc} = -0.5$ V *versus* solution; $WO_3$/liquid $E_{oc} = -0.73$ V *versus* $E^{0\prime}(O_2/H_2O)$). Optical concentration (12×, AM1.5D) shifted the open-circuit potential to $E_{oc} = -1.27$ V *versus* $E^{0\prime}(O_2/H_2O)$ and resulted in unassisted $H_2$ production during two-electrode measurements (anode: tandem device, cathode: Pt disc). The solar energy-conversion efficiencies were very low, 0.0068% and 0.0019% when the cathode compartment was saturated with Ar or $H_2$, respectively, due to the non-optimal photovoltage and band-gap of the $WO_3$ that was used in the demonstration system to obtain stability of all of the system components under common operating conditions while also insuring product separation for safety purposes.

### Broader context

Direct photoelectrochemical conversion of sunlight into a storable, energy-dense fuel has the opportunity to provide a predictable, carbon-neutral energy source to displace current carbon-based technologies. Solar hydrogen generation *via* water splitting is an important goal because the voltage requirements for this process are well matched to the maximum power point of high-efficiency tandem photovoltaics. In addition to including light-absorbing materials that provide sufficient voltage for water splitting, an integrated solar fuels device requires catalysts connected to the light absorbers and an ionic transport pathway between the anode and cathode to complete the circuit while maintaining product separation below the lower explosive limits, for safety purposes. Integration of these different active materials is important to further development of this technology. Single-crystalline Si microwire arrays represent an architecture that can allow the system operation and integration requirements to be met, because photoactive Si microwires have been previously embedded into ionically conductive, gas-blocking membranes. However, Si microwires do not produce enough photovoltage for unassisted water splitting even in a tandem Si-based structure. We describe a Si microwire based tandem junction device that produces sufficient photovoltage for unassisted water splitting, by use of $WO_3$ in a core–shell tandem structure. This system provides a proof-of-principle for this design, which can be improved significantly through the incorporation of higher efficiency wide band-gap semiconductors as they become available and are stable under the same conditions as the rest of the components of the device.

## Introduction

Si microwire array photocathodes have been shown to generate photovoltages in excess of 500 mV in acidic aqueous environments, and provide a preferred geometry, relative to planar structures, for devices that effect the unassisted generation of fuels from sunlight.[1–3] Microwire arrays benefit from orthogonalization of the directions of light absorption and minority-carrier collection,[4–8] as well as from light-trapping effects,[9,10] an increased surface area for catalyst loading per unit of geometric area,[11,12] a small solution resistance as compared to planar designs,[3,13] a reduced material usage through reusable substrates,[14] and the ability to embed the microwires into ion-exchange membranes that exhibit little permeability to $H_2$ and $O_2$,[15] thereby producing flexible devices that persistently separate the products of the water-splitting reaction. However, the voltage generated from single-junction Si microwire arrays is much lower than the 1.23 V required for solar-driven water splitting, so a wider band-gap partner light absorber must be introduced electrically in tandem (Si/partner tandem device), to generate useful current at voltages that exceed the thermodynamically required values for fuel production. Accordingly, tandem-junction devices offer the highest theoretical[16] and experimentally realized[7] efficiencies

[a]*Division of Chemistry and Chemical Engineering, California Institute of Technology, Pasadena, CA, USA. E-mail: nslewis@caltech.edu*

[b]*Joint Center for Artificial Photosynthesis, California Institute of Technology, Pasadena, CA, USA*

[c]*Thomas J. Watson, Sr. Laboratories of Applied Physics, California Institute of Technology, Pasadena, CA, USA*

† Electronic supplementary information (ESI) available. See DOI: 10.1039/c3ee43048k

for solar-driven water splitting through additive voltages across two photoabsorbers that effectively utilize multiple regions of the solar spectrum. Tandem device structures are also simpler to fabricate and operate effectively under a greater variety of insolation conditions than more complex 3- or 4-junction devices. Additionally, when kinetic overpotentials are considered in detail, water-splitting devices will most likely require a tandem architecture to achieve appreciable current densities, *i.e.* 10 mA $cm^{-2}$, thereby further motivating the use of tandem structures in such applications.

In addition to band gap considerations for a Si/partner tandem system, achieving the desired electronic behaviour at the interface between Si and its tandem partner presents a significant challenge for production of an integrated solar fuels generation device. The materials must be mutually compatible and generally must operate in a batch reactor that contains a single, concentrated (1.0 M)[3,17] aqueous electrolyte. Such materials considerations are important to the performance of a functioning device that consists of microwires embedded in a gas impermeable, ion-exchange membrane, because both semiconductors may need to be simultaneously in contact with the electrolyte to produce a full solar-driven water-splitting device. Tandem junction water-splitting devices using nanoscopic or microscopic materials have focused on a single-junction n–n heterojunction design in series with a liquid second junction.[18,19] In contrast, the highest efficiency water-splitting devices[7,20] consist of planar tandem homojunction photovoltaic cells that are physically isolated from the solution and are electrically connected to the catalysts in contact with solution. The materials currently used in high-efficiency planar tandem devices are not stable in concentrated aqueous electrolyte environments. Nevertheless, the concept of buried p–n homojunctions is a promising route to increase the efficiency of solar-driven water-splitting devices relative to systems that utilize n–n heterojunctions.[1,18,19,21,22] To realize the advantages of replacing the n–n heterojunction with a p–n homojunction, ohmic behaviour at the Si/tandem partner interface is required. This ohmic behaviour can be achieved in at least two ways: (i) the Si tandem partner must have a proper band alignment (type III, broken gap) such that upon direct contact, ohmic behaviour is produced or (ii) a discrete intermediate third material must be introduced that facilitates ohmic behaviour between the Si and the tandem partner light absorbers.

$TiO_2$, $WO_3$, $BiVO_4$ and $Fe_2O_3$ are stable in concentrated aqueous electrolytes and form suitable tandem partners for Si. However, Si is stable only in acidic aqueous environments, limiting the presently available partner materials that are stable under such conditions to only $TiO_2$ and $WO_3$. $WO_3$ is the preferred material because of its smaller band gap ($E_g \sim 2.6$ eV) and significant photocurrent response to visible-light illumination.[23] The electronic behaviour of the Si/$WO_3$ interface has recently been shown to be non-ohmic, but addition of an intermediate tin-doped indium oxide (ITO) layer has been shown to provide low resistance, ohmic behaviour between p-type, or $p^+$-type, Si and $WO_3$.[24] Thus, a Si/$WO_3$ microwire device with an intermediate ITO layer presents an opportunity to demonstrate an unassisted integrated solar-driven water-splitting device that exploits the advantages of the microwire-array architecture.

We describe herein a tandem core–shell photoelectrochemical device that consists of a periodic array of buried homojunction n–$p^+$-Si microwires that have been sequentially coated with a radial sheath of ITO and $WO_3$. When immersed in air-saturated 1.0 M $H_2SO_4$, the dual radial-junction microwire structure enables efficient carrier collection from both the Si and $WO_3$ light absorbers, despite short minority-carrier diffusion lengths, *i.e.*, ~10 μm in Si[25] and ~1 μm in $WO_3$. A necessary feature of this tandem architecture is the incorporation of the ITO layer between the Si and $WO_3$ light-absorbing materials. This ohmic contact layer ensures facile, low-resistance carrier transport between the Si and $WO_3$ and relaxes the requirements for proper band alignment between the $p^+$-Si emitter and the $WO_3$. Transparent conductive oxides, such as FTO or ITO, are commonly used as back contacts to semiconductor metal oxides; thus this design is expected to be robust towards implementation of newly discovered materials, because the ITO layer will be amenable to many different Si tandem partner absorbers.

# Experimental

### Chemicals

All chemicals were used as received unless noted otherwise. Water was filtered using a MilliPore system and had a resistivity >18 MΩ cm.

### Si microwire array growth

Phosphorous-doped ($N_D = 3 \times 10^{17}$ $cm^{-3}$) and boron-doped ($N_A = 1 \times 10^{17}$ $cm^{-3}$) Si microwire arrays were grown *via* a Cu-catalyzed vapor–liquid–solid (VLS) process on As-doped $n^+$-Si or on B-doped $p^+$-Si ⟨111⟩ wafers (<0.005 Ω cm, Addison).[2,6,25] The $n^+$-Si and $p^+$-Si ⟨111⟩ growth wafers were received with a 400 nm thick thermal oxide ($SiO_2$) that had been photolithographically patterned to produce 3 μm diameter holes filled with Cu in a square lattice (7 μm × 7 μm). The growth of Si microwire arrays was performed in a chemical-vapor deposition (CVD) furnace at atmospheric pressure using $SiCl_4$ (Strem, 99.9999+%) at 25 sccm flow rate, $H_2$ (Matheson, research grade) at 500 sccm flow rate, and $BCl_3$ (Matheson, 0.25% in $H_2$) at 1 sccm flow rate for 20 min or $PH_3$ (Matheson, 100 ppm in $H_2$) at 0.3 sccm flow rate for 9 min. Following growth, the samples were cooled to ~200 °C under a 500 sccm flow of He.

### Microwire array processing

Microwire arrays were cleaned using a 6 : 1 : 1 (by volume) $H_2O$ : HCl(fuming, aqueous) : $H_2O_2$(30% in $H_2O$) metal etch (RCA 2) for 20 min at 60 °C. The samples were then subjected to a 15 s etch in buffered HF(aq.) (BHF) etch, an $H_2O$ rinse, an organic (piranha) etch in 3 : 1 $H_2SO_4$(99.6%, aqueous) : $H_2O_2$(30% in $H_2O$) for 10 min at room temperature, and an $H_2O$ rinse. Following a 30 s etch in 10% BHF and a rinse with $H_2O$, a 150 nm thick $SiO_2$ layer was grown *via* dry thermal oxidation in a tube furnace at 1050 °C under an $O_2$ atmosphere

 

for 2.5 h. A 15 μm thick PDMS layer was deposited at the base of the wires by spin coating a solution, consisting of 1.1 g of polydimethylsiloxane (PDMS, Sylgard 185, Dow Corning) and 0.1 g of PDMS curing agent dissolved in 5 mL of toluene, on the sample at 3000 rpm for 30 s, followed by a 30 min cure in a vacuum oven at 150 °C. These PDMS-infilled arrays were submerged in BHF for 5 min, to remove the $SiO_2$ on the exposed microwire surfaces. The PDMS was removed by a 30 min soak in 3 : 1 *N*-methyl-2-pyrrolidone (NMP):tetrabutylammonium fluoride (TBAF, aq. 75 wt%), followed by a 30 s rinse with $H_2O$. The samples were then dried under a stream of $N_2$(g). Residual organics were then removed by a 10 min etch in a piranha solution.

### $p^+$-Si emitter formation on n-Si

A boron-doped $p^+$-Si radial emitter was formed on the n-Si microwire arrays and on planar ⟨111⟩ n-Si wafers (Silicon Inc., 0.7 Ω cm) by exposure of the samples in a CVD furnace to a 20 : 400 sccm flow of $BCl_3$ (Matheson, 0.25% in $H_2$) : $H_2$ (Matheson, research grade) at 950 °C for 30 min, immediately following a 30 s etch in 10% BHF. The samples were then rinsed with $H_2O$ and dried under a stream of $N_2$(g).

### ITO deposition

Immediately following a 15 s etch in 10% BHF, a rinse in $H_2O$ and drying under a stream of $N_2$(g), 400 nm of In-doped tin oxide was sputtered (48 W, 3 mTorr, 20:0.75 sccm Ar: 10% $O_2$ in Ar) onto n–$p^+$-Si microwire arrays and p-Si microwire arrays, by DC magnetron sputtering under 10 W of substrate bias (to facilitate conformal deposition on the microwire sidewalls). The thickness of the ITO was determined by spectroscopic ellipsometry measurements on a planar Si sample.

### $WO_3$ deposition

n-$WO_3$ was electrodeposited from a tungstic peroxy-acid solution, as described previously.[26] Briefly, 4.6 g of tungsten powder (0.6–1 μm, 99.99%, Sigma Aldrich) was dissolved in a molar excess (60 mL) of $H_2O_2$ (30% in $H_2O$). Excess $H_2O_2$ was decomposed by addition of a trace amount of Pt black (99.9%, Sigma Aldrich) for 24 h. The $H_2O_2$ concentration was monitored by peroxide test strips (EM Quant) until the final peroxide concentration was <30 ppm. A concentrated stock solution was made by addition of 80 mL of $H_2O$ and 60 mL of isopropyl alcohol (IPA) to the as-made solution. To increase the lifetime of the solution, the stock solution was protected from light and stored at 2 °C in a refrigerator. A 3 : 7 IPA : $H_2O$ mixture was used to dilute the stock solution (3 : 2 IPA–$H_2O$ mix : stock solution) to generate the deposition solution. Stock solutions were used for one week and thereafter were freshly prepared. All ITO-coated samples were used as prepared for deposition of $WO_3$, and were contacted directly to the ITO layer using a flat alligator clip. Deposition of $WO_3$ on n–$p^+$-Si and p-Si microwire arrays was performed potentiostatically at −0.5 V *vs.* Ag/AgCl for 60 min. After deposition, all samples were annealed in air at 400 °C for 2 h. This process formed monoclinic $WO_3$, as confirmed by X-ray diffraction data.

### Electrode fabrication

Three types of electrodes were tested: n–$p^+$-Si microwire arrays; n–$p^+$-Si/ITO/$WO_3$ microwire arrays; and p-Si/ITO/$WO_3$ microwire arrays. To make ohmic contact to Si substrates that supported the microwire arrays, In-Ga (99.99%, Alfa-Aesar) eutectic was scratched into the back side of the samples. Exposed In-Ga (Si electrodes) was affixed to a coiled Cu–Sn wire with Ag paint (SPI 05001-AB). The active area (~0.12 $cm^2$ for Si microwire arrays) was defined with epoxy (Loctite Hysol 9460) and the entire electrode was sealed with epoxy to the bottom of a glass tube (6 mm O.D.). The electrode orientation, down- or side-facing, was determined by the orientation of the coiled wire that protruded from the glass tube. Geometric areas were measured by scanning the active area, and using software (ImageJ) to calculate the area.

### Non-aqueous photoelectrochemistry

Bottom-facing electrodes that contained n–$p^+$-Si microwire arrays were etched for 30 s in 10% BHF immediately prior to introducing the samples into a glove box. Solutions for photoelectrochemical measurements consisted of $CH_3CN$ (anhydrous, 99.8%, Sigma Aldrich) distilled under $N_2$(g) (ultra-high purity, Air Liquide) from calcium hydride ($CaH_2$), 1 M $LiClO_4$ (battery grade, 99.99%, Sigma Aldrich), and either 25 mM bis(cyclopentadienyl) iron(II) (ferrocene, $FeCp_2^0$, Sigma Aldrich) and 3 mM bis(cyclopentadienyl) iron(III) tetrafluoroborate (ferrocenium, $FeCp_2^+ \cdot BF_4^-$, Sigma Aldrich), or 20 mM bis(cyclopentadienyl) cobalt(II) (cobaltocene, $CoCp_2^0$, Sigma Aldrich) and 2 mM bis(cyclopentadienyl) cobalt(III) hexafluorophosphate (cobaltocenium, $CoCp_2^+ \cdot PF_6^-$, Sigma Aldrich). Cobaltocene and ferrocene were purified by vacuum sublimation at room temperature, and cobaltocenium and ferrocenium were recrystallized prior to use. An ELH-type W–halogen lamp with a dichroic rear reflector was used for illumination, and was set to produce the same current density on a calibrated Si photodiode as was obtained from 100 mW $cm^{-2}$ of 1 Sun AM1.5G illumination. Three-electrode photoelectrochemical data were obtained in a single-compartment cell by use of a Gamry potentiostat (Reference 600), with a Pt counter electrode and a Pt quasi-reference electrode at a scan rate of 20 mV $s^{-1}$.

### Aqueous photoelectrochemistry

Side-facing planar and microwire array (p-Si/ITO/$WO_3$, n–$p^+$-Si/ITO/$WO_3$) devices were tested in 1 M $H_2SO_4$(aq.) (trace metal grade, Fischer Scientific) saturated with air. Multiple devices were tested (>5) with the reported results representing the best performing devices. Two-electrode and three-electrode measurements were conducted using a Biologic (SP-200) potentiostat in a two-compartment cell (whose compartments are referred to as the anode compartment and the cathode compartment) that contained an epoxied (Loctite Hysol 1C) quartz window on the anode side and a Nafion® (0.05 mm thick, Alfa Aesar) membrane separator between the compartments. Illumination was produced by a Xe lamp (Oriel 67005, Newport Instruments) with an AM1.5G filter (Newport

Instruments 81094) that produced light intensities of either 1 (100 mW $cm^{-2}$) or 12 (1080 mW $cm^{-2}$) Suns on a calibrated Si photodiode. The concentration value (12×) was determined using the AM1.5D spectrum to be consistent with what would be expected in outdoor testing, although an AM1.5G source was used. Calibration was performed such that the cited light intensity was the highest light intensity anywhere in the cell and the position of the photodiode at this light intensity was marked to assure that the sample was positioned at the same point as the photodiode. Optical concentration was achieved using a plano-convex lens (Thorlabs LA4984). The spot size (~1 $cm^2$) overfilled all of the samples tested (~0.1 $cm^2$ in area).

### Three-electrode measurements

Three-electrode measurements were conducted at a scan rate of 20 mV $s^{-1}$ with the working electrode in the anode compartment open to air, an SCE reference electrode (CH Instruments, CHI150) in the anode compartment, and a Pt mesh counter electrode in the cathode compartment. Pt disc (0.0314 $cm^2$) three-electrode measurements were performed with the Pt disc in the cathode compartment and with the SCE reference and the Pt mesh counter electrodes in the anode compartment. For Pt disc measurements, the cathode compartment was saturated with either Ar(g) (research grade, Air Liquide) or $H_2$(g) (research grade, Air Liquide) by bubbling the gas through the solution for 15 min before testing, as well as throughout the experiment. All of the measurements were referenced to the potential of the regular hydrogen electrode (RHE) ($E(H^+/H_2)$), obtained empirically using the Pt disc electrode under 1 atm of $H_2$(g), −0.247 V *vs.* SCE.

### Two-Electrode measurements

Two-electrode measurements were made in the same two-compartment cell as used for the three-electrode measurements and with the electrodes in the same physical location. The cathode compartment was purged with Ar(g) or $H_2$(g). A Pt disc electrode was used as the cathode, to simulate the expected catalyst area for an integrated device. The anode compartment contained the working electrode, which was illuminated through a quartz window and was open to air. Chronoamperometric measurements were taken under potentiostatic control at 0 V applied bias between the photoanode and cathode.

### Load-line analysis

The Pt disc current versus potential (*I*–*E*) data were mirrored about the abscissa, to facilitate straightforward evaluation of the projected electrochemical operating conditions of the device. The Pt disc data included the solution and membrane resistances, because during the measurement the reference electrode was in the opposite cell from the Pt electrode. Hence, the Pt disc data should account for all of the expected cell resistances in the system of interest. The predicted operating currents from the load-line analysis were calculated based on the average of the forward and reverse scans and were $6.7 \times 10^{-3}$ mA ($6.1 \times 10^{-2}$ mA $cm^{-2}$) and $2.6 \times 10^{-3}$ mA ($2.1 \times 10^{-2}$ mA $cm^{-2}$) for the Ar(g)- and $H_2$(g)-saturated solutions, respectively. The current densities were calculated per geometric surface area of the electrode and were determined using Fig. 5a. Efficiencies were calculated using the Gibbs free energy for water splitting ($\Delta E^0 = 1.23$ V) into $H_2$(g) and $O_2$(g) at standard conditions to obtain the energy content of the fuel produced, and the known irradiance (12 suns AM1.5D, 1080 mW $cm^{-2}$).

### Product analysis

Oxidation products (peroxydisulfate ($S_2O_8^{2-}$)) generated at the $WO_3$/1.0 M $H_2SO_4$ interface were detected using an ultraviolet-visible spectrophotometer (Agilent 8453, 1 cm quartz cuvette) as reported previously.[26] Calibration curves were determined using potassium peroxydisulfate ($K_2S_2O_8$).

Reduction products ($H_2$(g)) generated at the Pt disc/1.0 M $H_2SO_4$ interface were detected using a mass spectrometer (Hiden Analytical HPR-20 QIC). Current was passed through the Pt disc electrode for 40 min under identical conditions (identical electrochemical cell, current (−6.5 μA), solution (trace metal grade 1.0 M $H_2SO_4$) and Ar(g) purge) as used in the two-electrode experiment described above. The experiment was started only after obtaining a steady background signal for $m/z = 2$.

### Light absorption simulation

1D and 2D light absorption was simulated in Lumerical FDTD, a commercially available Maxwell's equation solver that uses the FDTD method. The software requires material-specific refractive index data (Table S1 and Fig. S1†). The experimentally fabricated microwire structures were reproduced in the Lumerical workspace in 2D. Bloch boundary conditions were used to model an infinite planar structure and an infinite 2D microwire array. Each structure was illuminated with single-wavelength plane waves with the electric field polarized in the 2D structured plane, at wavelengths ranging from 350 to 1100 nm in 50 nm intervals. Partial spectral averaging was used to remove simulation artifacts that were caused by the use of single-wavelength simulations. The structure was meshed with 20 mesh boxes per wavelength. The spatially resolved electric field, $E$, and complex refractive index ($\varepsilon$) were recorded and then used to calculate the spatially resolved carrier generation rate, $C_{gen}$ (eqn (1)):

$$C_{gen} = \frac{\pi |E|^2 \mathrm{imag}(\varepsilon)}{h} \quad (1)$$

where $h$ is Planck's constant. The spatially resolved carrier generation rate was used as the optical input for the electronic simulations. The power absorbed in each material was calculated by integrating the spatially resolved absorbed power, $P_{abs}$ (eqn (2)).

$$P_{abs} = -0.5\omega |E|^2 \mathrm{imag}(\varepsilon) \quad (2)$$

The absorbed photon flux in each material as a function of wavelength was weighted with the AM1.5G spectrum, integrated over wavelength, and multiplied by Faraday's constant to obtain a short-circuit current density assuming unity internal quantum

 

yield (IQY). The concentrated illumination modeling was performed at 11 Suns using the AM1.5G spectrum to match the experimental photon flux of 12× of AM1.5D.

### n–p$^+$-Si junction modeling

Electronic device simulations were performed in Synopsys Sentaurus, a commercially developed software package that solves the drift–diffusion equation for charge carriers using a finite-element method. For simplicity, a single n–p$^+$-Si homojunction and an n-$WO_3$/($O_2$/$H_2O$) liquid junction were modeled separately. The built-in materials parameter file for Si was used with modified time constants ($\tau_n(N_A = 10^{20}\ cm^{-3}) = 3 \times 10^{-6}$ s; $\tau_p(N_D = 10^{17}\ cm^{-3}) = 1 \times 10^{-3}$ s), with $\tau_n$ and $\tau_p$ being the electron and hole lifetime, respectively, and $N_A$ and $N_D$ being the acceptor and donor concentrations, respectively. The silicon n–p$^+$ junction was constructed with a 100 μm thick n-region with $N_D = 10^{17}\ cm^{-3}$ and a 0.2 μm thick p$^+$-region with $N_A = 10^{20}\ cm^{-3}$. In the quasi-neutral bulk of the n-Si, a standard mesh size of 500 nm and 5 μm was used transverse and parallel to the junction, respectively. Near the ohmic contact with n-Si, the mesh was refined to 500 nm and 100 nm, and near the junction, the mesh was refined to 500 nm and 20 nm, to accurately model the band bending in these regions. The *J–E* (current density *vs.* potential) characteristics of this structure were obtained by first solving for the $V = 0$ case in the dark. Subsequently, the voltage was stepped at 0.010 V intervals in both the positive and negative directions, to obtain the dark *J–E* behaviour. The carrier-generation rate from Lumerical was then applied to extract the *J–E* characteristics in the presence of illumination. Similarly, the $V = 0$ case in the light was solved first, and then the voltage was stepped at 0.010 V intervals, to obtain the light *J–E* performance. Shockley–Read–Hall recombination was used for all simulations.

### $WO_3$/liquid junction modeling

The built-in "oxide as semiconductor" materials parameter file was used to model $WO_3$, with the following parameters and their values in parentheses: modified band gap ($E_g = 2.6$ eV), work function ($\chi = 4.4$ eV), relative permittivity ($\varepsilon_r = 5.76$), effective conduction- and valence-band density of states ($N_C = 1.8 \times 10^{19}\ cm^{-3}$, $N_V = 7.1 \times 10^{19}\ cm^{-3}$), recombination time constant ($\tau_n = \tau_p = 1 \times 10^{-8}$ s) and mobility ($\mu_n = \mu_p = 40\ cm^2\ V^{-1}\ s^{-1}$). The band gap was experimentally measured from absorption measurements using an integrating sphere and a Tauc plot. The relative permittivity was calculated from ellipsometric measurements of the complex refractive index. The work function was chosen based on reports in the literature.[27] The density of states can be calculated from $m^*$, the effective mass of holes in the valence band and of electrons in the conduction band, $k_B$, the Boltzmann constant, $h$, the Planck constant and $T$, the temperature (eqn (3)):

$$N_c = 2\left(\frac{2\pi m_e^* k_B T}{h^2}\right)^{3/2} \quad (3)$$

Effective masses in the conduction band have been reported to be ~0.8 $m_0$,[28] where $m_0$ is the mass of a free electron. Density functional theory calculations of the band structure of $WO_3$ indicate that the valence band has less curvature than the conduction band, indicating heavier holes and leading to an estimate of 2 $m_0$ for the hole effective mass.[29] The mobility values were also taken from the literature.[28] Preliminary experimental measurements indicated a diffusion length of 1 μm, thereby determining the time constant.

The $WO_3$/liquid junction was modeled as a Schottky junction, with the metal work function equal to the water oxidation redox potential, $\chi = 5.68$ eV, which was in contact with a 1 μm thick slab of $WO_3$. A value of $N_D = 10^{15}\ cm^{-3}$ was chosen to match the experimentally observed short-circuit current density and open-circuit voltage. Mesh sizes of 10 nm and 250 nm were used perpendicular and parallel to the junction, respectively. The method to obtain the dark and light *J–E* behaviour was identical to that used for modeling the Si junction. Shockley-Read-Hall recombination and thermionic emission physics were used for these simulations.

### Hydrogen-evolution catalysis modeling

Butler–Volmer kinetics in the absence of mass-transport limitations were used with a Tafel slope, $\alpha = 1$ and an exchange current density, $j_0 = 10^{-3}\ A\ cm^{-2}$, to simulate the cathodic overpotential (eqn (4)) of platinum (Pt) for hydrogen evolution in 1.0 M $H_2SO_4$:

$$\eta = -\frac{RT}{F}\ln\left(\frac{j}{j_0} + 1\right) \quad (4)$$

Where $R$ is the gas constant, $T$ is the absolute temperature, and $F$ is Faraday's constant. The overpotential, $\eta$, was added to the n–p$^+$-Si homojunction *J–E* data at the same current density to yield a simulated hydrogen generation device curve in the absence of mass transport.

## Results

Fig. 1a–f depicts the process used to fabricate the on-wafer devices used herein. Fig. 1g displays an image of a completed wire-array device, while Fig. 1h shows a cross-section of a single wire demonstrating the layered device structure. The Si microwires were 40–70 μm in length, had a diameter of ~2 μm and had doping densities on the order of $10^{17}\ cm^{-3}$. Secondary-ion mass spectrometry data from planar samples (Fig. S2†) indicated that the p$^+$-Si emitter thickness was ~200 nm. The sequential, conformal layers of ITO and $WO_3$ were ~100 nm and ~400 nm, respectively. Fig. S3† and Fig. S4† further confirm the layered structure of the tandem microwire device using EDX analysis.

### Device design

Fig. 2a shows the core–shell Si/$WO_3$ microwire array design, and Fig. 2b shows an individual two-dimensional unit cell of the design. The highly doped p$^+$-Si sheath surrounds a moderately doped n-Si microwire core, creating a radial n–p$^+$-Si buried

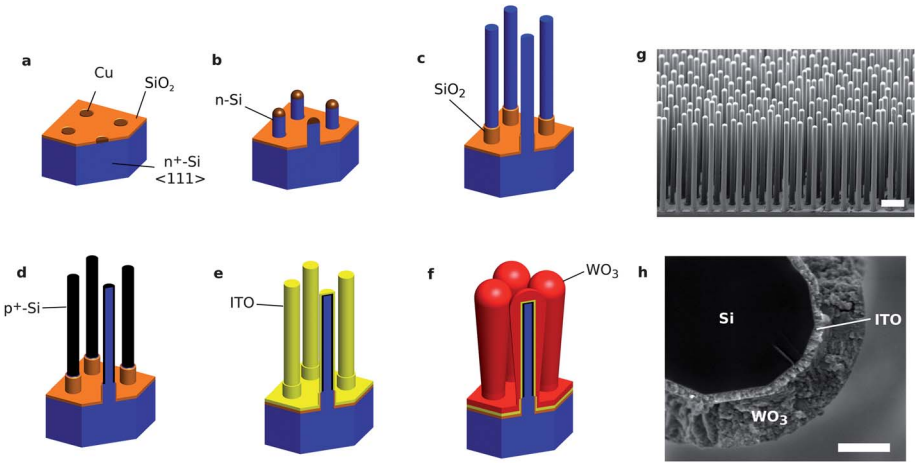


Fig. 1 (a) Photolithographically patterned $n^+$-Si ⟨111⟩ wafer with a $SiO_2$ mask layer and Cu catalyst in the desired growth pattern. (b) VLS Cu-catalyzed growth of n-type Si microwires on an $n^+$-Si substrate followed by a metal etch (RCA 2). (c) $SiO_2$ diffusion barrier (boot) formation *via* $SiO_2$ growth, PDMS infill, HF etch and PDMS removal. (d) $p^+$-Si emitter drive-in from $BCl_3$ precursor at 950 °C for 30 min in a CVD furnace. (e) Conformal DC sputter coating of ITO. (f) Conformal n-$WO_3$ electrodeposition and annealing at 400 °C for 2 h. (g) Fully assembled tandem junction device array SEM (scale bar = 10 μm). (h) Cross-sectional SEM of a fully assembled tandem junction single wire demonstrating the layered structure of the device (scale bar = 500 nm).

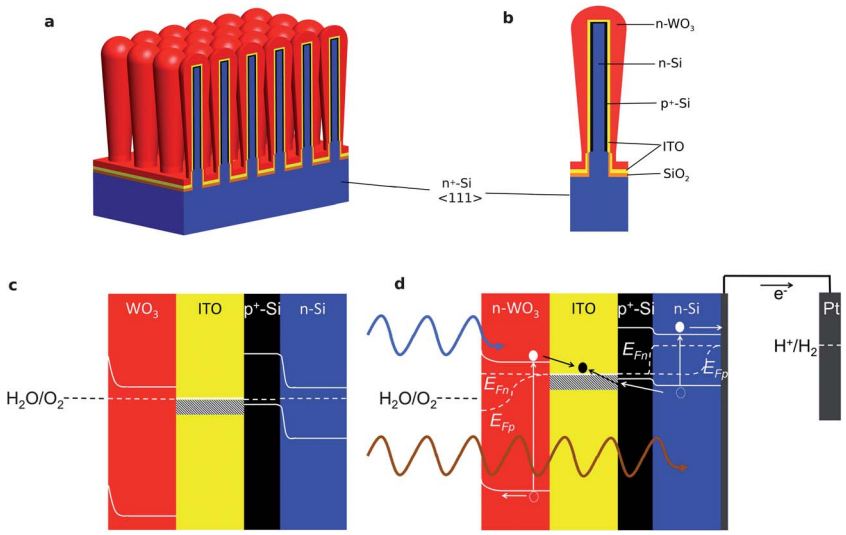


Fig. 2 (a) Tandem junction microwire array with a buried homojunction (n–$p^+$-Si) coated by ITO and n-$WO_3$. (b) 2D cross-section of an individual tandem junction array unit cell. (c) Electronic structure of the tandem device in the dark showing the buried n–$p^+$-Si junction, ohmic Si/ITO/n-$WO_3$ junction, and n-$WO_3$/liquid junction. The device is shown equilibrated with the oxygen-evolution potential. (d) Steady-state electronic structure of the tandem device under illumination with the carrier movement directions shown. Both the oxygen- and hydrogen-evolution potentials are shown, with the overpotentials accounted for by the difference between the respective quasi-Fermi level and reaction potential. Electrons and holes are collected radially in the n-$WO_3$. Holes are collected radially in the n–$p^+$-Si and electrons are collected axially at the back contact.

junction. A conformal layer of ITO surrounds the $p^+$-Si, forming a transparent ohmic contact between the $p^+$-Si and the conformal layer of n-$WO_3$. A liquid junction is formed between the $WO_3$ and the solution redox couple (shown as the potential of the oxygen-evolution reaction (OER)).

Fig. 2c and d depict the device electronic band structures in the absence and presence of illumination, respectively. Illumination (Fig. 2d) results in splitting of the quasi-Fermi levels at both junctions, generating two voltage sources in series. Photoexcited majority-carrier electrons in the n-Si core are transported axially to the back contact through the degenerately doped substrate ($n^+$-Si) to perform the hydrogen-evolution reaction (HER) at a Pt counter electrode, while photoexcited minority-carrier holes are collected radially in the $p^+$-Si sheath. The holes in Si recombine with photoexcited majority-carrier electrons from the n-$WO_3$ at the ITO contact, while minority-carrier holes that are photoexcited in the n-$WO_3$ are collected at the liquid interface and drive the oxidation of water or anolyte.[26]

 

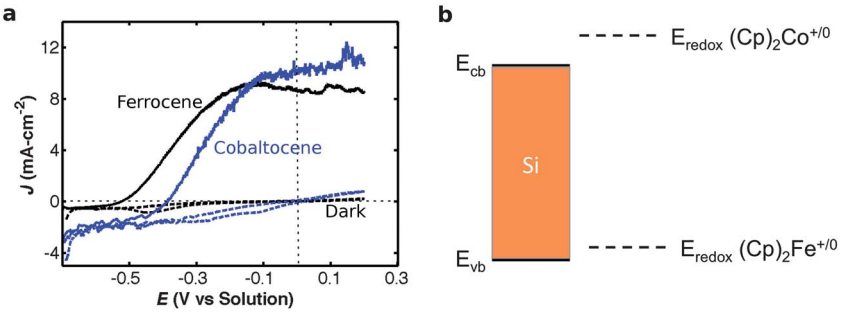


Fig. 3 (a) Non-aqueous photoelectrochemical (forward scan, scan rate = 20 mV-s$^{-1}$) results using ferrocene$^{+/0}$ ($(Cp)_2Fe^{+/0}$) and cobaltocene$^{+/0}$ ($(Cp)_2Co^{+/0}$) as redox couples to probe the n–p$^+$-Si buried junction performance in microwire arrays. The dark scans are dashed lines and the light scans are shown as solid lines. (b) Redox potentials of cobaltocene and ferrocene with respect to the potentials of the conduction-band edge and the valence-band edge of Si.

During the course of this work, a similar, yet distinct, device that performs unassisted solar-driven water splitting was reported that incorporates a p–n$^+$-Si nanowire junction connected to $TiO_2$ by the p-Si nanowire core (referred to as Si/$TiO_2$).[22] One major difference between the device design presented here (referred to as Si/$WO_3$) and the Si/$TiO_2$ design is the collection probability of excess charge carriers in Si. Excess minority carriers are collected radially throughout the Si wire for the Si/$WO_3$ design, maintaining collection lengths (<2 μm) shorter than reported minority-carrier diffusion lengths (~10 μm).[25,30] Conversely, excess minority carriers are collected axially in the top half of the Si/$TiO_2$ design, requiring collection lengths much longer than the largest diffusion lengths measured in Si microwires (~10 μm).[25,30] Optical absorption modeling of Si microwires indicates that a majority of the incident light is absorbed near the top of the wire, emphasizing the need for efficient minority-carrier collection in this region.[31] Si nanowires also have excessive junction area that leads to high rates of carrier recombination relative to Si microwires.[4] These differences are apparent when comparing the open-circuit voltage values for the Si/$TiO_2$ device (370 mV) and the Si/$WO_3$ device (480 mV). The Si/$TiO_2$ device utilized two masking steps to define the structure and a top-down fabrication process that began with a high-quality photo-active p-Si wafer, whereas fabrication of the Si/$WO_3$ device consisted of sequential deposition of the active materials with a single masking step and featured a bottom-up fabrication process from a reusable photo-inactive n$^+$-Si substrate.[14]

### n–p$^+$-Si microwire non-aqueous photoelectrochemistry

The performance of individual buried junction n–p$^+$-Si microwire array devices was investigated through non-aqueous photoelectrochemical measurements in contact with a series of one-electron, outer-sphere redox couples (Fig. 3). The cobaltocene$^{+/0}$ ($CoCp_2^{+/0}$) and ferrocene$^{+/0}$ ($FeCp_2^{+/0}$) redox species were used to determine the quality of the buried junction, by probing the n- and p-type character at the Si–liquid interface. Fig. 3b displays the redox potentials of $CoCp_2^{+/0}$ and $FeCp_2^{+/0}$ with respect to the potentials of the Si conduction and valence bands. The p$^+$-Si radial sheath is expected theoretically, and was observed experimentally, to form an ohmic contact to $FeCp_2^{+/0}$ and to form a tunnel junction to $CoCp_2^{+/0}$. For a fully buried junction, similar performance should therefore be observed in contact with both of these redox systems. However exposed n-Si is expected theoretically and, is observed experimentally, to form an electrical short (*i.e.*, an ohmic contact) to $CoCp_2^{+/0}$ and a rectifying contact to $FeCp_2^{+/0}$.

In contact with $FeCp_2^{+/0}$ under 100 mW cm$^{-2}$ of simulated AM1.5G illumination, the n–p$^+$-Si microwire array devices exhibited an open-circuit potential of $E_{oc} = -0.5$ V *versus* solution, and a short-circuit current density of $J_{sc} = 8.7$ mA cm$^{-2}$, with a fill factor of 0.44 (Fig. 3a). Similar performance was observed for microwire structures in contact with $CoCp_2^{+/0}$ indicating that the performance is due to the buried n–p$^+$-Si junction.

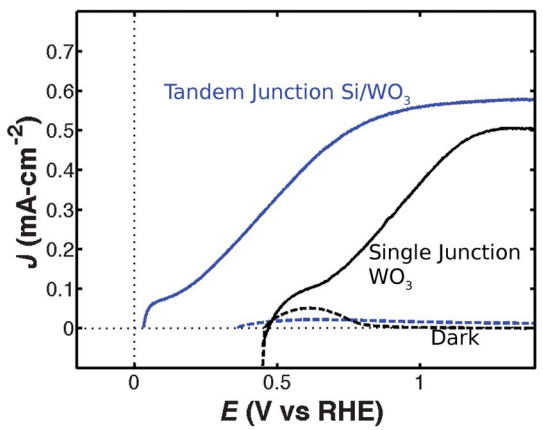


Fig. 4 Three electrode photoelectrochemical (forward scan, scan rate = 20 mV s$^{-1}$) performance for single (black) and tandem (blue) junction microwire devices in contact with 1.0 M $H_2SO_4$(aq.). The single junction microwire device consisted of $WO_3$ supported on p-Si microwires that had been coated with ITO. Here the p-Si/ITO contact is ohmic so the only rectifying junction is at the $WO_3$/liquid junction. These data demonstrate the presence of an additive voltage from each junction, with 0.73 V and 0.5 V produced by the $WO_3$/liquid and n–p$^+$-Si buried junctions, respectively. The $E_{oc}$ for the single junction device was defined as the point at which the dark current, due to capacitive charging, and the illuminated current separated. The $E_{oc}$ for the tandem junction device was defined as the point at which no current was flowing because no positive dark current existed in this region.

The 0.1 V decrease in $E_{oc}$ observed for the $CoCp_2^{+/0}$ contact compared to the $FeCp_2^{+/0}$ contact is consistent with the presence of exposed n-Si near the $SiO_2$/Si boundary (boot) creating an electrical short to solution.[12] This is important to note, however it has been shown that the n-Si/ITO interface produces a barrier rather than an electrical short like n-Si/$CoCp_2^{+/0}$.[24] Thus, the n–$p^+$-Si-microwire part of the ultimate tandem structure is expected to contribute $V_{oc}$ = 0.5 V and is not expected to limit the current of the tandem device, because the maximum possible $J_{sc}$ from $WO_3$ is ~5 mA $cm^{-2}$.[32]

### Single ($WO_3$) and tandem (Si/$WO_3$) junction photoelectrochemistry

Fig. 4 shows the photoelectrochemical behaviour of single junction (p-Si/ITO/n-$WO_3$/1.0 M $H_2SO_4$) and tandem junction (n-Si/$p^+$-Si/ITO/n-$WO_3$/1.0 M $H_2SO_4$) microwire array devices under simulated one Sun illumination conditions. The p-Si/ITO and $p^+$-Si/ITO contacts have been shown to produce ohmic behaviour allowing isolation of the n-$WO_3$/1.0 M $H_2SO_4$ liquid junction performance in the single junction case and efficient use of the buried n–$p^+$-Si junction in the tandem junction case.[24] The single- and tandem-junction microwire devices exhibited $J$ = 0.50 mA $cm^{-2}$ and $J$ = 0.58 mA $cm^{-2}$, respectively, at the formal potential for oxidation of water to $O_2$, $E^{o\prime}(O_2/H_2O)$. The first peak in photocurrent density is a dark redox process that results in the photochromism of $WO_3$, whereupon reverse scans the $WO_3$ film is reduced through proton intercalation, and is subsequently oxidized on the forward scan. The second peak is associated with photocurrent that results in actual solution redox reactions. The slightly lower current density exhibited by the single junction is consistent with decreased absorption due to the use of shorter microwire arrays. For comparison, Fig. S5† displays data from the planar equivalent of these microwire devices.

The open-circuit potentials were $E_{oc}$ = −0.73 V *vs.* $E^{o\prime}(O_2/H_2O)$ and $E_{oc}$ = −1.21 V *vs.* $E^{o\prime}(O_2/H_2O)$ for the single- and tandem-junction devices, respectively. The $E_{oc}$ for the $WO_3$/liquid contact is in accord with expectations for $WO_3$ photoanodes operating under these conditions.[19] The 0.48 V shift in $E_{oc}$ of the tandem junction device relative to the single junction device is therefore attributable to the presence of the n–$p^+$-Si buried junction in the tandem device (Fig. 3). This voltage shift demonstrates that the buried n–$p^+$-Si junction increases the voltage generated by Si as compared to n-Si/n-type metal–oxide heterojunction devices.[18,19]

### Load-line analysis

Under modest optical concentration (12 Suns, AM1.5D), tandem junction microwire-array devices exhibited $E_{oc}$ = −1.27 V *vs.* $E^{o\prime}(O_2/H_2O)$, which exceeds the 1.23 V potential difference necessary for unassisted water splitting under standard-state conditions (Fig. 5a and S6†). The operating current for this device under modest optical concentration can be predicted using a load-line analysis.[33] Fig. 5a shows the *I–E* behaviour of an illuminated tandem microwire device, along with the *I–E* behaviour, mirrored about the abscissa, of a Pt disc

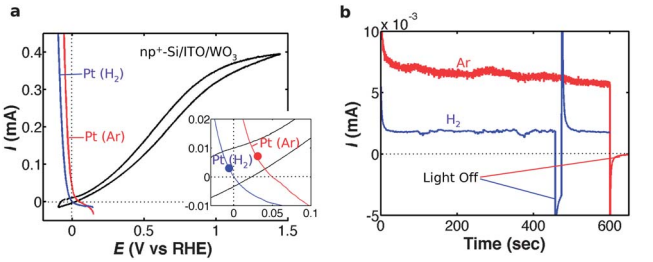


Fig. 5 (a) *J–E* curves and load-line analysis of the tandem junction (n–$p^+$-Si/ITO/$WO_3$) microwire device at 12 suns (AM1.5D) plotted against the dark HER curves (mirrored about the abscissa) using a Pt disc electrode in an Ar(g)- or $H_2$(g)-saturated solution. These measurements were conducted in a two-electrode cell with 1 M $H_2SO_4$ in both compartments separated by a Nafion membrane to maintain product separation. The Pt disc HER curves include solution and membrane resistances because the reference electrode (SCE) was placed in the opposite cell at the same location used for the tandem microwire array device. The inset is a zoomed-in view around the operational points, which are indicated by the red (Ar) and blue ($H_2$) circles. (b) Two-electrode measurements at 0 V applied bias between the tandem junction device (concentrated illumination) and Pt disc electrode in either Ar(g)- or $H_2$(g)-saturated solution. Turning the light off, as indicated, demonstrated that the positive current was photoinduced.

electrode of similar projected area, in contact with either a saturated Ar(g) or $H_2$(g) solution at 1 atm. In an Ar(g)-saturated solution, the onset potential for the HER was shifted positive compared to that observed in a $H_2$(g)-saturated solution, in accordance with Le Châtelier's principle. These data were obtained using a two-compartment cell (Fig. S7†) with a Nafion membrane separating the anode and cathode compartments. The *I–E* behaviour of the Pt disc includes the solution and membrane resistances of the electrochemical cell, because the reference electrode was placed in the opposite (anode) compartment. This type of measurement provides a robust prediction of the unassisted operating current that should be obtained between an illuminated Si/$WO_3$ microwire array device and a Pt button electrode in the same geometry and physical location. The anolyte was not purged with $O_2$ because the primary oxidation product from $WO_3$ under these conditions has been shown to be peroxydisulfate.[21]

Fig. 5b displays the chronoamperometric response from a two-electrode experiment at 0 V applied bias between an illuminated tandem junction $WO_3$/Si microwire array device and a Pt disc electrode. The devices produced solar-to-hydrogen energy-conversion efficiencies of 0.0068% ($6.5 \times 10^{-3}$ mA, 0.060 mA $cm^{-2}$) and 0.0019% ($1.9 \times 10^{-3}$ mA, 0.017 mA $cm^{-2}$) when the Pt disc was in contact with Ar(g)- and $H_2$(g)-saturated solutions, respectively, which agree with the predicted operating points from the load-line analysis (dots at intersection points in Fig. 5 insets). The peroxydisulfate/sulfate redox system has a formal reduction potential that is ~0.75 V positive of $E^{o\prime}(O_2/H_2O)$, indicating that the tandem core–shell microwire device generated ~1.8 V of photopotential under these conditions. Device photostability was demonstrated for over 10 min by the $H_2$(g)-purged device. Thus, the decrease in current for the Ar(g)-purged device is attributable to an increasing $H_2$ concentration in solution from the HER at the Pt disc electrode.

 

Additionally, the chopped-light response demonstrated that the observed current was photo-induced. The negative current observed in the dark for the $H_2$(g)-purged device is consistent with $O_2$ (g) and $H_2$(g) recombination to form water, similar to fuel cell operation. This behaviour demonstrates that the operating voltage of the device can be tuned by changing the partial pressures of the photoelectrochemical reaction products, *i.e.* by changing the chemical load across the device, which can be calculated using the Nernst equation.

### Product analysis

Product analysis was performed separately on the oxidation and reduction products in 1.0 M $H_2SO_4$. As reported previously, electrolyte buffer species are oxidized preferentially at the $WO_3$/liquid interface, relative to the oxidation of water.[26] Thus, in contact with $H_2SO_4$(aq.), sulfate ($SO_4^{2-}$) is preferentially oxidized to peroxydisulfate ($S_2O_8^{2-}$), which was confirmed as an oxidative product by ultraviolet-visible absorption spectroscopy as published previously.[26] Although direct oxygen evolution was not realized due to the slow $O_2$ evolution kinetics of $WO_3$, peroxydisulfate has been shown to stoichiometrically evolve $O_2$ using $Ag^+$ as a catalyst.[26]

At the Pt disc cathode, $H_2$(g) production was detected by mass spectrometry of the reaction products when the operational current density was passed at the Pt disc electrode (Fig. S8†). Due to the small amount of $H_2$(g) produced, direct quantification of the faradaic efficiency was not performed, however no other products are expected due to the use of trace metal grade $H_2SO_4$.

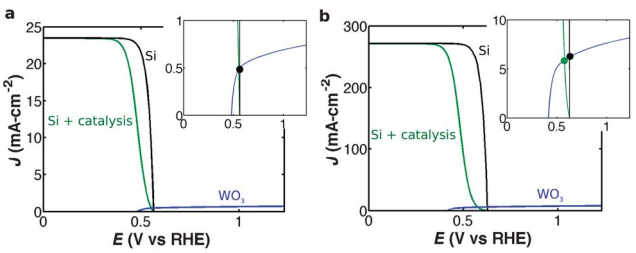


Fig. 6 Modeled $J$–$E$ data and load-line analysis for unconcentrated (a) and concentrated (b) illumination conditions that match the experimental photon fluxes at 1 and 12 Suns (AM 1.5D). The Si homojunction is shown with (green) and without (black) inclusion of realistic hydrogen-evolution catalytic overpotentials. Butler–Volmer kinetics with $\alpha = 1$ and $j_0 = 10^{-3}$ A cm$^{-2}$ was used to calculate the catalytic overpotentials in the absence of mass-transport limitations. The insets show the operating point for unconcentrated illumination (black dot) and for concentrated illumination, with (green dot) and without (black dot) overpotentials due to HER catalysis included. The rate of catalysis is not expected to affect the $WO_3$ $J$–$E$ behaviour due to the large band gap of $WO_3$ and the proximity of $E^{o\prime}(O_2/H_2O)$ to the potential of the conduction band of $WO_3$.

### 1D optoelectronic model

Fig. 6 shows the $J$–$E$ behaviour and simulated load-line analyses of the one-dimensional device architecture (Fig. S9†) in the bulk recombination limit under both unconcentrated (1 Sun) and concentrated illumination sufficient to match the experimental photon flux (see Fig. S10† for the individual $J$–$E$ behaviour of the Si and $WO_3$ junctions). Here, the Si homojunction performance is shown in the absence of mass-transport limitations, with and without the incorporation of catalytic overpotentials ($\eta$) associated with the HER, which are present in any actual water-splitting device. The maximum predicted operating points from this analysis are 0.5 mA cm$^{-2}$ (Fig. 6a inset) and 5.7 mA cm$^{-2}$ (Fig. 6b inset) for unconcentrated (one Sun) and concentrated illumination, respectively. This corresponds to an $E_{oc} = -1.29$ V *vs.* $E^{o\prime}(O_2/H_2O)$ for unconcentrated illumination and $E_{oc} = -1.44$ V *vs.* $E^{o\prime}(O_2/H_2O)$ for concentrated illumination. Fig. S11† compares the modeled and experimentally measured $J$–$E$ behaviour for a Pt electrode performing the HER under 1 atm of $H_2$. The differences arise from the exclusion of mass transport and series resistance in the model.

### 2D microwire optical modeling

Table 1 shows the light-limited photocurrent densities ($J_{ph}$) that were calculated assuming unity internal quantum yield (IQY) for the tandem structure for varying $WO_3$ coating thicknesses: (i) the entire device (Si and $WO_3$), (ii) only $WO_3$, and (iii) $WO_3$ coating the microwire sidewalls only. Fig. S12† shows the simulated carrier-photogeneration-rate maps for photons with energy larger than the $WO_3$ band-gap energy (~2.6 eV, 476 nm). Table S2† lists the geometric parameters used, based on the structure depicted in Fig. 2b.

## Discussion

### Tandem junction performance

The $E_{oc} = -1.27$ V *vs.* $E^{o\prime}(O_2/H_2O)$ exhibited by the tandem junction n–p$^+$-Si/ITO/n-$WO_3$ microwire array device indicates that the structure provides enough voltage to drive unassisted

Table 1 Dependence of the light-limited photocurrent density ($J_{ph}$) on the $WO_3$ coating thickness for light above the $WO_3$ band gap (<476 nm) in: (i) all photoactive material in the core–shell tandem structure (Si + $WO_3$), (ii) $WO_3$ and (iii) $WO_3$ on the microwire sidewalls only ($WO_3$ on microwire). $J_{ph}$ is calculated assuming unity IQY.

| $WO_3$ Thickness (nm) | Geometric filling fraction (%) | Si + $WO_3$ $J_{ph}$ <476 nm (mA cm$^{-2}$) | $WO_3$ $J_{ph}$ (mA cm$^{-2}$) | $WO_3$ on microwire $J_{ph}$ (mA cm$^{-2}$) |
|---|---|---|---|---|
| 300 | 11.7 | 3.34 | 0.56 | 0.41 |
| 500 | 15.4 | 3.43 | 0.7 | 0.54 |
| 700 | 19.6 | 3.47 | 0.8 | 0.65 |
| 1000 | 26.9 | 3.53 | 0.89 | 0.79 |
| 1500 | 41.7 | 3.52 | 1.08 | 1.07 |

solar-driven water splitting under standard-state conditions and 12 Suns illumination (AM1.5D). Additionally, $H_2(g)$ was detected as a reduction product confirming unassisted hydrogen production. To realize a complete, direct water-splitting device, an oxygen-evolution catalyst coupled to the $WO_3$ surface would be required. Two-electrode operation with a Pt HER electrode demonstrated stable operation of the device as well as validation of the operating point determined by the load-line analysis. This demonstration therefore provides a proof-of-concept for the development of core–shell high-aspect ratio tandem junction devices for fuel formation directly from sunlight. Such a device could be embedded in a gas-impermeable, ion-selective membrane[15] and removed from a reusable substrate[14] to form a free-standing device. This architecture minimizes the distance ions must travel to complete the fuel-forming circuit, thus minimizing the potential drop due to solution resistance effects.

### 1D optoelectronic modeling

The performance of the tandem junction n–$p^+$-Si/ITO/n-$WO_3$ device described herein is fundamentally limited in two ways by $WO_3$: (i) its wide band gap ($\sim$2.6 eV) limits the maximum current density to $\sim$5 mA $cm^{-2}$ under AM1.5G illumination conditions; and (ii) the barrier height between $WO_3$ and $E^{o\prime}(O_2/H_2O)$ limits the $E_{oc}$ to less than half of the band gap. Given these two limitations, a one-dimensional optoelectronic model (Fig. S9†) for the tandem structure was developed to investigate the maximum performance that could be expected from the Si/$WO_3$ device and can be compared to the experimental results.

The modeled $E_{oc}$ values are 80 mV and 170 mV larger, respectively, than the experimentally observed $E_{oc}$ values, which can be ascribed to an increased junction area ($\sim$9$\times$) in the experiment as compared to the planar model. These open-circuit potential differences manifest themselves as large differences between the modeled and experimental two-electrode operating points due to the proximity of the modeled operating point to the maximum power point in the $WO_3$ *J–E* behaviour; any unaccounted resistances and/or open-circuit potential losses between the model and experiment, such as junction area, will therefore cause a precipitous decrease in the experimental operating current density. This effect is observed in both experimental illumination conditions, where under one Sun illumination the $E_{oc}$ is less than 1.23 V such that the device cannot perform unassisted water splitting at standard conditions. Under concentrated illumination the experimental $E_{oc}$ exceeds 1.23 V, but is lower than the modeled value and explains the cause for the difference in operating points.

### 2D optical modeling

As shown in Fig. 2a and b, $WO_3$ forms a conformal coating on the Si microwires and the planar, degenerately doped Si base, all of which can result in photocurrent. To investigate the photocurrent contribution from $WO_3$ on the microwire sidewalls relative to that from $WO_3$ on the planar, degenerately doped Si base, two-dimensional finite-difference time domain (FDTD) electromagnetic modeling was performed on the structure presented in Fig. 2b. Table 1 demonstrates that for thin $WO_3$ coatings (300 nm), only 17% (0.56 mA $cm^{-2}$) of the above band-gap light absorbed by the device is absorbed in the $WO_3$. The $WO_3$ absorption fraction increases to 31% (1.08 mA $cm^{-2}$) for thicker $WO_3$ coatings (1.5 μm). The carrier-generation-rate maps (Fig. S12†) demonstrate that the majority of the $WO_3$ absorption is within the top 10 μm of the device, with many photons whose energies are larger than the energy of the $WO_3$ band gap transmitted through the $WO_3$ to the underlying Si, where absorption is not useful due to the current-limiting absorption in the $WO_3$. This behaviour implies that an alternative $WO_3$ geometry is desired to enhance the $WO_3$ absorption. However, a device geometry designed to increase the $WO_3$ absorption should optimally accommodate the $\sim$1 μm minority-carrier diffusion length of $WO_3$, implying the beneficial use of $WO_3$ layers <1 μm thick.

For 300 nm thick $WO_3$ coatings, 73% of the total $WO_3$ optical absorption occurred in $WO_3$ on the sidewalls of the Si microwires. This absorption fraction increased to 99% for 1.5 μm thick $WO_3$ coatings; the 500 nm thick $WO_3$ coatings used experimentally are projected at $\sim$76%. This substantial fraction of absorption along the sidewalls *versus* at the bottom of the device architecture indicates that similar performance is expected for on-wafer microwires compared to free-standing microwire array devices that have been removed from the growth wafer, which will be a crucial step for integration of this tandem device into a fully functional solar fuels generator. Additionally, scattering particles could be introduced to redirect more light toward the microwire sidewalls for enhanced $WO_3$ absorption.[1,10]

### Toward higher efficiency devices

Integration of new photoanode materials in place of $WO_3$ has the potential to increase the performance of the tandem device by producing more negative $E_{oc}$ values as well as much larger values of the current density at $E = E^{o\prime}(O_2/H_2O)$. To produce a more negative value of $E_{oc}$, the potential of the conduction band of the anode material must be more negative than the potential of the conduction band of $WO_3$, *i.e.* closer to the vacuum level, thereby increasing the barrier height at the semiconductor/liquid junction. Recent studies of mixed-metal oxides have demonstrated photoanode materials with smaller electron affinities than $WO_3$.[34–36] The production of increased current density at $E = E^{o\prime}(O_2/H_2O)$ will require lowering the recombination rates, by improving the material quality and passivating surface states, as well as the discovery of narrower band-gap materials that are stable under oxidizing conditions. Additionally the anodes must be stable under conditions where the cathode and membrane materials are stable, and under conditions where the membrane exhibits high transference numbers for protons, to allow for effective, passive neutralization of the pH gradient between the sites of water oxidation and water reduction while maintaining product separation for intrinsically safe operation of the system under varying levels of illumination.

 

## Conclusions

A $Si/WO_3$ integrated tandem junction device capable of unassisted solar-driven water-splitting has been developed and used to demonstrate unassisted hydrogen evolution under moderate light concentration. This system provides proof-of-principle for the design. The approach is attractive because it provides materials flexibility for the Si tandem partner absorber, an optimized electrochemical geometry, embedment in a flexible, gas-impermeable, ion-exchange membrane and enhanced absorption and carrier-collection properties relative to planar designs. The $Si/WO_3$ described herein demonstrated additive voltages across the tandem device resulting in an $E_{oc} = -1.21$ V *vs.* $E^{o\prime}(O_2/H_2O)$. Modest optical concentration (12 Suns) produced a shift in $E_{oc}$ to potentials negative of $E^{o\prime}(H_2O/H_2)$, indicating that the device could split water in an unassisted fashion. Two-electrode measurements performed with no applied bias between the photoanode and a Pt disc cathode resulted in hydrogen production at current densities of 0.060 mA $cm^{-2}$ and 0.017 mA $cm^{-2}$ when the catholyte was saturated with Ar(g) and $H_2$(g), respectively. These operating points agreed well with the values that were predicted from the load-line analysis based on separate measurements of the performance of the cathodic and photoanodic electrodes. The low energy-conversion efficiencies result from a highly non-optimal band gap and photovoltage of the $WO_3$/liquid contact, and much higher efficiencies could be obtained if an alternative suitable photoanode system were identified that was also stable under conditions where the remainder of the system was stable.

## Acknowledgements

This material is based upon work performed by the Joint Center for Artificial Photosynthesis, a DOE Energy Innovation Hub, supported through the Office of Science of the U.S. Department of Energy under Award Number DE-SC0004993. M.S. acknowledges the Resnick Sustainability Institute for a graduate fellowship. K.F. is supported by the National Science Foundation Graduate Research Fellowship under Grant No. DGE-1144469. S.A. acknowledges support from a U.S. Department of Energy, Office of Energy Efficiency and Renewable Energy (EERE) Postdoctoral Research Award under the EERE Fuel Cell Technologies Program. The authors would like to thank Dr Shu Hu for assistance in boron doping, Rick Gerhart for fabrication of the electrochemical cells used and Dr Andrew Leenheer for the $WO_3$ refractive index data.

## References

1 S. W. Boettcher, E. L. Warren, M. C. Putnam, E. A. Santori, D. Turner-Evans, M. D. Kelzenberg, M. G. Walter, J. R. McKone, B. S. Brunschwig, H. A. Atwater and N. S. Lewis, *J. Am. Chem. Soc.*, 2011, **133**, 1216–1219.
2 S. W. Boettcher, J. M. Spurgeon, M. C. Putnam, E. L. Warren, D. B. Turner-Evans, M. D. Kelzenberg, J. R. Maiolo, H. A. Atwater and N. S. Lewis, *Science*, 2010, **327**, 185–187.
3 S. Haussener, C. Xiang, J. M. Spurgeon, S. Ardo, N. S. Lewis and A. Z. Weber, *Energy Environ. Sci.*, 2012, **5**, 9922–9935.
4 B. M. Kayes, H. A. Atwater and N. S. Lewis, *J. Appl. Phys.*, 2005, **97**, 114302.
5 M. H. Lee, K. Takei, J. Zhang, R. Kapadia, M. Zheng, Y.-Z. Chen, J. Nah, T. S. Matthews, Y.-L. Chueh, J. W. Ager and A. Javey, *Angew. Chem., Int. Ed.*, 2012, **51**, 10760–10764.
6 J. R. Maiolo, B. M. Kayes, M. A. Filler, M. C. Putnam, M. D. Kelzenberg, H. A. Atwater and N. S. Lewis, *J. Am. Chem. Soc.*, 2007, **129**, 12346–12347.
7 O. Khaselev and J. A. Turner, *Science*, 1998, **280**, 425–427.
8 H. J. Lewerenz, *Photoelectrochemical Materials and Energy Conversion Processes*, Wiley-VCH Verlag GmbH & Co. KGaA, Weinheim, Germany, 2010, vol. 12.
9 J. M. Rubi and S. Kjelstrup, *J. Phys. Chem. B*, 2003, **107**, 13471–13477.
10 M. D. Kelzenberg, S. W. Boettcher, J. A. Petykiewicz, D. B. Turner-Evans, M. C. Putnam, E. L. Warren, J. M. Spurgeon, R. M. Briggs, N. S. Lewis and H. A. Atwater, *Nat. Mater.*, 2010, **9**, 239–244.
11 A. G. Muñoz, C. Heine, M. Lublow, H. W. Klemm, N. Szabo, T. Hannappel and H. J. Lewerenz, *ECS J. Solid State Sci. Technol.*, 2013, **2**, Q51–Q58.
12 E. L. Warren, J. R. McKone, H. A. Atwater, H. B. Gray and N. S. Lewis, *Energy Environ. Sci.*, 2012, **5**, 9653.
13 C. Xiang, A. C. Meng and N. S. Lewis, *Proc. Natl. Acad. Sci. U. S. A.*, 2012, **109**, 15622–15627.
14 J. M. Spurgeon, K. E. Plass, B. M. Kayes, B. S. Brunschwig, H. A. Atwater and N. S. Lewis, *Appl. Phys. Lett.*, 2008, **93**, 032112.
15 J. M. Spurgeon, M. G. Walter, J. Zhou, P. A. Kohl and N. S. Lewis, *Energy Environ. Sci.*, 2011, **4**, 1772.
16 J. Bolton, S. Strickler and J. S. Connolly, *Nature*, 1985, **316**, 495–500.
17 Y. Zhao, E. S. Smotkin and T. Mallouk, *Energy Environ. Sci.*, 2012, **5**, 7582–7589.
18 Y. J. Hwang, A. Boukai and P. Yang, *Nano Lett.*, 2009, **9**, 410–415.
19 M. T. Mayer, C. Du and D. Wang, *J. Am. Chem. Soc.*, 2012, **134**, 12406–12409.
20 S. Licht, B. Wang, S. Mukerji, T. Soga, M. Umeno and H. Tributsch, *J. Phys. Chem. B*, 2000, **104**, 8920–8924.
21 E. L. Warren, S. W. Boettcher, M. G. Walter, H. A. Atwater and N. S. Lewis, *J. Phys. Chem. C*, 2011, **115**, 594–598.
22 C. Liu, J. Tang, H. M. Chen, B. Liu and P. Yang, *Nano Lett.*, 2013, **13**, 2989–2992.
23 X. Liu, F. Wang and Q. Wang, *Phys. Chem. Chem. Phys.*, 2012, **14**, 7894.
24 R. H. Coridan, M. Shaner, C. Wiggenhorn, B. S. Brunschwig and N. S. Lewis, *J. Phys. Chem. C*, 2013, **117**, 6949–6957.
25 M. D. Kelzenberg, D. B. Turner-Evans, M. C. Putnam, S. W. Boettcher, R. M. Briggs, J. Y. Baek, N. S. Lewis and H. A. Atwater, *Energy Environ. Sci.*, 2011, **4**, 866.
26 Q. Mi, A. Zhanaidarova, B. S. Brunschwig, H. B. Gray and N. S. Lewis, *Energy Environ. Sci.*, 2012, **5**, 5694–5700.
27 A. Subrahmanyam and A. Karuppasamy, *Sol. Energy Mater. Sol. Cells*, 2007, **91**, 266–274.

28 J. M. Berak and M. J. Sienko, *J. Solid State Chem.*, 1970, **2**, 109–133.
29 H. Jin, J. Zhu, J. Hu, Y. Li, Y. Zhang, X. Huang, K. Ding and W. Chen, *Theor. Chem. Acc.*, 2011, **130**, 103–114.
30 M. C. Putnam, D. B. Turner-Evans, M. D. Kelzenberg, S. W. Boettcher, N. S. Lewis and H. A. Atwater, *Appl. Phys. Lett.*, 2009, **95**, 163116.
31 M. Kelzenberg, *Silicon Microwire Photovoltaics. Ph.D. Thesis*, The California Institute of Technology, 2010.
32 Z. Chen, T. F. Jaramillo, T. G. Deutsch, A. Kleiman-Shwarsctein, A. J. Forman, N. Gaillard, R. Garland, K. Takanabe, C. Heske, M. Sunkara, E. W. McFarland, K. Domen, E. L. Miller, J. A. Turner and H. N. Dinh, *J. Mater. Res.*, 2010, **25**, 3–16.
33 M. G. Walter, E. L. Warren, J. R. McKone, S. W. Boettcher, Q. Mi, E. A. Santori and N. S. Lewis, *Chem. Rev.*, 2010, **110**, 6446–6473.
34 J. A. Seabold and K.-S. Choi, *J. Am. Chem. Soc.*, 2012, **134**, 2186–2192.
35 S. P. Berglund, A. J. E. Rettie, S. Hoang and C. B. Mullins, *Phys. Chem. Chem. Phys.*, 2012, **14**, 7065–7075.
36 H. S. Park, K. E. Kweon, H. Ye, E. Paek, G. S. Hwang and A. J. Bard, *J. Phys. Chem. C*, 2011, **115**, 17870–17879.